



HAL
open science

Damping performance of finite microperforated plates using multi-sized and spacial distributions of perforations

Lucie Gallerand, Mathias Legrand, Thomas Dupont, Philippe Leclaire

► **To cite this version:**

Lucie Gallerand, Mathias Legrand, Thomas Dupont, Philippe Leclaire. Damping performance of finite microperforated plates using multi-sized and spacial distributions of perforations. 2023. hal-04122565v1

HAL Id: hal-04122565

<https://hal.science/hal-04122565v1>

Preprint submitted on 8 Jun 2023 (v1), last revised 2 May 2024 (v3)

HAL is a multi-disciplinary open access archive for the deposit and dissemination of scientific research documents, whether they are published or not. The documents may come from teaching and research institutions in France or abroad, or from public or private research centers.

L'archive ouverte pluridisciplinaire **HAL**, est destinée au dépôt et à la diffusion de documents scientifiques de niveau recherche, publiés ou non, émanant des établissements d'enseignement et de recherche français ou étrangers, des laboratoires publics ou privés.



Distributed under a Creative Commons Attribution 4.0 International License

Damping performance of finite microperforated plates using multi-sized and spacial distributions of perforations

Lucie Gallerand^a, Mathias Legrand^b, Thomas Dupont^a, Philippe Leclaire^c

^a*Department of Mechanical Engineering, École de technologie supérieure, Montréal, Canada*

^b*Department of Mechanical Engineering, McGill University, Montréal, Canada*

^c*DRIVE EA1859, Université de Bourgogne, ISAT, Nevers, France*

In the context of structural dynamics, recent works by the authors showed that microperforations can be used to mitigate vibration. Microperforated plates (MPPs) have been shown to exhibit substantial added damping stemming from fluid-structure interactions and visco-thermal effect mechanisms in the boundary layers of the perforations during relative motion between the solid and the fluid contained in the perforations. The added damping reaches a maximum for a characteristic frequency, depending only on the perforation diameter. Choosing the perforation diameter so that the characteristic frequency coincides with the natural frequency of the plate reduces the mode contribution of the plate. However, the studied MPPs had a single set of perforations homogeneously distributed over the structure. It is proposed in this work to broaden the frequency band and maximize the added damping using MPPs with multi-sized perforation diameters and optimized spatial distribution of perforations. As an extension of the previous vibratory model by the author, the dynamics of MPPs with multi-sized perforation based on a homogenization model is established. In addition, the effect of the spacial distribution of perforations on the additional damping is captured by including a spatially dependent perforation ratio in the model. Experimental measurements on MPPs validate the proposed analytical models. The results show that: (i) MPPs with multiple size perforations exhibit a broader effective damping frequency band; (ii) the added damping enhances when the perforations are distributed in the area of the antinodes of the considered mode. Thus, by coupling the two effects, it is possible to achieve MPPs that effectively reduce the vibratory responses on several modes.

Keywords: Microperforated plate — Additional damping — Multiple perforation sizes — Gradients of properties

Contents

1	Introduction	1
2	MPP with homogeneous perforation	3
2.1	Vibration model	3
2.2	Added damping	4
3	MPP with multi-sized microperforations	5
3.1	Homogenization model	5
3.2	Experimental validation	7
4	MPP with spacial distribution of perforations	8
4.1	Perforation ratio gradient	8
4.2	Experimental validation	11
5	MPP with multi-sized perforations and spacial distribution of perforations	12
6	Conclusion	14

1. Introduction

Microperforated plates (MPPs) are usually employed as lightweight acoustic absorbers for noise reduction and are regarded as an alternative to conventional porous materials or conventional acoustic resonators. MPPs can be used in many fields to reduce noise, such as meeting room [1, 13], acoustic coatings in flow ducts [29] or nuclear engines and reactors [28] for example. These simple structures can be safe,

Email addresses: lucie.gallerand.1@ens.etsmtl.ca (Lucie Gallerand), mathias.legrand@mcgill.ca (Mathias Legrand), thomas.dupont@etsmtl.ca (Thomas Dupont), philippe.leclaire@u-bourgogne.fr (Philippe Leclaire)

environment-friendly and can be made of different materials. They can be designed to be resistant to harsh environments, translucent or biodegradable. MPPs transform acoustic energy into heat by exchanges in the viscous and thermal boundary layers near the fluid-solid interface of the microperforations.

The acoustic properties of microperforated plates were investigated through various models, including models based on the Kirchhoff equations [17] and equivalent fluid models such as the Johnson-Allard approach [10, 3]. The vibrations of MPPs were also considered with the aim to investigate their influence on the acoustic properties of structures [26, 11, 7]¹. Research was also conducted to improve and extend MPPs' acoustic absorption by using different partitioned cavity depths [25] or multi-sized perforation [19, 14], i.e., an MPP whose perforations have various diameters. Indeed, Kim and Yoon [14] proposed a configuration of a multi-sized microperforation in order to improve MPP's absorption and to achieve wideband frequency absorption. An electro-acoustic equivalent circuit method was used to explore the sound absorption properties of a perforated panel with microperforated partitions [8, 9]. Qian *et al.* [24] also used an electro-acoustic equivalent circuit method to model a multi-sized microperforations. They proposed a multi-population genetic algorithm to optimize the design of multi-size MPP absorbers. Theoretical results showed that only a multi-sized MPP absorber with grouped perforations can improve the sound absorption capability of MPPs. Mosa *et al.* [20] explored the absorption coefficient of an inhomogeneous MPP with multi-cavity depths. Results showed that introducing an inhomogeneous perforation improved the absorption capability of an MPP absorber compared to a homogeneous one. Experimental and numerical studies have also been performed in an acoustic MPP context with multi-sized perforation diameters. Miasa *et al.* [19] explored experimentally the sound absorption performance of a microperforated plate with multi-sized perforation diameters. The results showed that multi-sized MPP absorbers can exhibit high sound absorption over a wider frequency range than uniformly sized MPPs. The authors also concluded that in the case of an MPP with multiple perforation diameters, the benefits of each MPP with a single perforation size were combined. Qian and Zhang [23] used finite element analysis to investigate the influence of an MPP with multi-sized perforation diameters on the normal absorption performance of the parallel MPP absorber. Some authors have also conducted research on the effect of perforation distribution on the sound absorption of MPPs. Temiz *et al.* [27] proposed to numerically explore the effect of perforation distribution on sound absorption by assuming that perforations are discrete impedance patches, as proposed in [21, 18]. Although their works focused on MPP sound absorption, they observed that the distribution of perforations on the MPP could have a significant effect on the viscous damping mechanism. Different diameters and perforation arrangements were modelled using the finite element method and then via an experimental study [22]. They observed that the perforation ratio and the perforation position have an influence on the dynamics of the plate.

In addition to the acoustics, the structural dynamics of MPP was also explored. A recent work by the authors [12], and based on [15] and [3], has shown, both theoretically and experimentally, that energy dissipation at the fluid-solid interface in the microperforations. Parametric studies have demonstrated the existence of a single characteristic frequency, which depends on the constant diameter of the perforation and the perforation ratio, at which the added damping reaches a maximum. Accordingly, if the characteristic frequency coincides with the frequency of a plate mode, the mode will be mitigated by the added damping. On the other hand, the added damping will be weaker on the other natural modes. Its impact will be all the more limited as their frequencies are far from the characteristic frequency. An MPP with several perforation sizes and therefore with several characteristic frequencies (one for each perforation diameter) should theoretically have an optimized added damping on each of the modes having a frequency close to one of the characteristic frequencies of the plate. Moreover, additional damping capabilities are due to viscous frictions and thermal exchanges in the boundary layers occurring during the motion of the structure. It is therefore expected that more perforations distributed over the areas where the structural displacement is maximum will induce a magnified added damping. The present work proposes to improve and enhance the additional damping presented by microperforations by using multi-sized perforation diameters and a spacial distribution of perforations.

In this paper, each section proposes to study a different type of MPP, as listed below:

Section 2 MPP with uniform perforation corresponding to the reference MPP;

Section 3 MPP with multi-sized perforation diameters;

Section 4 MPP with spacial perforation distribution;

Section 5 MPP with multi-sized and spacial perforation distribution.

For each section, a model and experimental validations are proposed. To this end, it is firstly proposed to recall in **Section 2** the governing equations of the dynamic of a thin MPP saturated by a lightweight fluid already detailed in [12]. The model used to capture the effect of multi-sized perforation diameters in

¹For a more detailed literature review on the acoustics and vibroacoustics of uniform MPPs, the reader is invited to refer to the introduction in [12].

Section 3 is based on a homogenization approach. In Section 4, the spatial distribution of perforations is considered by defining a spatial perforation ratio. Section 5 proposes to combine the two models presented in Section 3 and Section 4. Finally, conclusions are given in Section 6.

2. MPP with homogeneous perforation

2.1. Vibration model

The previous work [12] by the authors developed a vibration model of a finite-size MPP of dimensions $L_x \times L_y \times h$, as illustrated in Figure 1, obtained by identifying the MPP with a porous plate and using an alternative form of the Biot's theory [4, 15]. It is used again in the present work, but multi-sized and spacially distributed microperforation are considered in Sections 3 to 5. Bending only is accounted for and the MPP is regarded as a homogeneous plate excited by an external load of the form $f_{\text{ext}}(x, y, t)$.

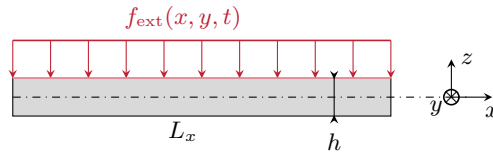


Figure 1: System of coordinates for an equivalent solid plate excited by an external mechanical force along z -axis.

Under a low-frequency assumption, the dynamic response of an MPP saturated by a lightweight fluid is solution to the two coupled governing equations [12]

$$\left(D + \frac{\alpha^2 M_f h^3}{12}\right) \nabla^4 w_s(x, y, t) + h(\rho \ddot{w}_s(x, y, t) + \rho_f \ddot{w}(x, y, t)) = f_{\text{ext}}(x, y, t), \quad (1a)$$

$$\alpha M_f \nabla^2 w_s(x, y, t) + \left(\rho_f \ddot{w}_s(x, y, t) + \frac{\rho_f \alpha_\infty}{\phi^{(0)}} \ddot{w}(x, y, t)\right) + \sigma^{(0)} \dot{w}(x, y, t) = 0, \quad (1b)$$

where ∇ is the vector differential operator so that $\nabla^2(\cdot) = \frac{\partial^2(\cdot)}{\partial x^2} + \frac{\partial^2(\cdot)}{\partial y^2}$ and $\nabla^4(\cdot) = \nabla^2(\cdot)^2$. The relative fluid-solid motion is $w(x, y, t) = \phi^{(0)}(w_f(x, y, t) - w_s(x, y, t))$ with $w_f(x, y, t)$, the fluid displacement and $w_s(x, y, t)$, the solid displacement and $\phi^{(0)}$ is the perforation ratio. Note that there was a sign error in [12] but this had no impact on the results presented. The equation system is corrected in this paper. Equation (1a) models the elastic response of the equivalent non-perforated homogeneous solid plate and Equation (1b), the relative fluid-solid motion in the perforations. The coefficient D is the bending stiffness defined as a function of the plate thickness h , Young's modulus E and Poisson's ratio of the non-perforated structure ν . In order to capture the effect of the microperforation on the response of the plate, Young's modulus E should be adapted to account for the effect of perforations on the plate rigidity [6, 12]. The bending stiffness therefore depends on $\phi^{(0)}$ as follows:

$$D = \frac{Eh^3}{12(1-\nu^2)} \frac{(1-\phi^{(0)})^2}{1+(2-3\nu)\phi^{(0)}}. \quad (2)$$

For a vibrating MPP saturated by a lightweight fluid, the elastic modulus of the plate is much greater than that of the fluid i.e., $E \gg M_f$: accordingly, $D + \frac{\alpha^2 M_f h^3}{12} \approx D$ in Equation (1) and in the remainder of the paper. The density of fluid-solid mixture is captured by $\rho = (1 - \phi^{(0)})\rho_s + \phi^{(0)}\rho_f$ where ρ_s and ρ_f are the solid and fluid densities, respectively. In Equation (1b), M_f corresponds to the elastic modulus of the equivalent fluid. The dimensionless quantity α characterizes the elastic coupling between the equivalent fluid and the solid. In the context of an MPP saturated by a lightweight fluid, we have $\alpha M_f \approx K_f$ [15] where K_f is the fluid bulk modulus. With the above assumptions, Equation (1) becomes (temporal and spatial dependencies are omitted)

$$D \nabla^4 w_s + h(\rho_s(1 - \phi^{(0)})\ddot{w}_s + \rho_f \phi^{(0)}\ddot{w}_f) = f_{\text{ext}}, \quad (3a)$$

$$\alpha M_f \nabla^2 w_s + \rho_f((1 - \alpha_\infty)\ddot{w}_s + \alpha_\infty \ddot{w}_f) + \sigma^{(0)} \phi^{(0)}(\dot{w}_f - \dot{w}_s) = 0. \quad (3b)$$

Porous parameters used in Biot's theory (resistivity $\sigma^{(0)}$, perforation ratio $\phi^{(0)}$ and tortuosity α_∞) are, for an MPP, functions of d , the perforation diameter and the airflow resistivity reads [3]

$$\sigma^{(0)} = \frac{\varsigma}{\phi^{(0)}} \quad \text{with} \quad \varsigma = \frac{32\mu_f}{d^2} \quad (4)$$

where μ_f is the dynamic viscosity of the fluid. In order to consider the distortion of the airflow in the perforations and fluid-solid interactions between perforations, an empirical correction on [3]

$$\alpha_\infty = 1 + B(1 - 1.14\sqrt{\phi^{(0)}}) \quad \text{with} \quad B = \frac{0.48}{h}\sqrt{\pi d^2} \quad (5)$$

is applied on both sides of the plate thickness [3]. In Equation (5), the term in parentheses contains the edge interaction between neighboring perforations.

2.2. Added damping

MPP feature interactions in viscous and thermal boundary layers associated with fluid-solid interactions, known to induce a non-neglecting additional damping in the plate [12]. This phenomenon reaches a maximum at the characteristic frequency

$$f_c = \frac{32\mu_f}{2\pi\alpha_\infty\rho_f d^2} \quad (6)$$

defined from Biot's frequency for porous materials [4, 15]. In Equation (6), f_c depends only on the perforation diameter d and the fluid parameters ρ_f and μ_f . The perforation diameter d can be adapted to induce maximum added damping at a resonance frequency, that is in a manner where f_c coincides with a natural frequency of the plate. The additional damping provided by the microperforations is largest at the characteristic frequency, but also acts in a frequency range centred on f_c .

Figure 2 depicts the damping capabilities of an MPP: the forced responses of aluminum simply-supported MPP of dimension $490 \text{ mm} \times 570 \text{ mm} \times 1 \text{ mm}$ and the corresponding non-perforated plate are compared. The perforation diameter of the MPP is set to $d = 1.6 \text{ mm}$ in order to induce maximum added damping on the first MPP mode. The perforation ratio is set to $\phi^{(0)} = 10 \%$. The vibration attenuation

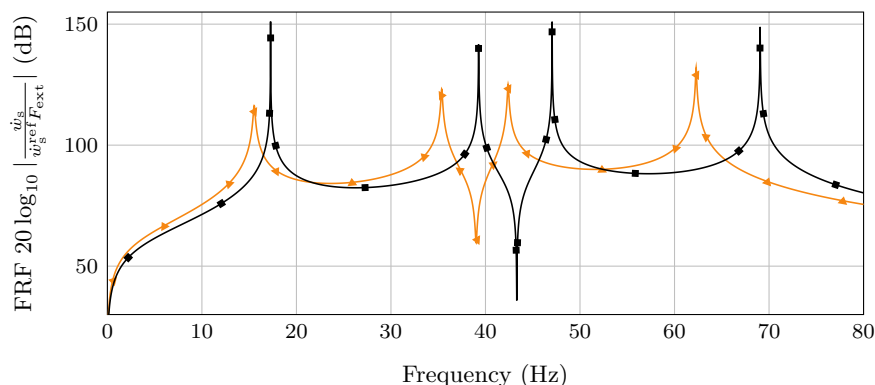


Figure 2: Mobility for two aluminum plates of dimensions $490 \text{ mm} \times 570 \text{ mm} \times 1 \text{ mm}$: (—■) reference non-perforated plate; (—▲) MPP with perforation diameter set to induce a maximum added damping at the first MPP natural frequency. Perforation parameters are $d = 1.6 \text{ mm}$ and $\phi^{(0)} = 10 \%$. Velocity reference is $\dot{w}_s^{\text{ref}} = 1.3 \times 10^{-6} \text{ m/s}$. Isotropic structural factor of aluminum $\eta_s = 10^{-4}$ is also considered.

and the loss factor for each MPP resonance frequency are listed in Table 1. The loss factor η_{mn} is related to the modal damping factor ζ_{mn} by the following expression $\eta_{mn} = 2\zeta_{mn}$ at the eigenfrequency. The modal damping factor ζ_{mn} is obtained for the m, n mode after solving Equation (1) via a modal analysis as detailed in [12]. The vibration attenuation Y_{mn} is determined by the absolute difference between the MPP amplitude at the resonance frequency m, n and that obtained for the non-perforated plate. The shift

m, n	$\eta_{mn} [\times 10^{-3}]$	$\Delta Y_{mn} \text{ (dB)}$
1, 1	10.64	38
1, 2	3.46	30
2, 1	2.52	27
2, 2	1.20	21

Table 1: Modal damping factor ζ_{mn} and amplitude reduction ΔY_{mn} for mode mn of a simply supported MPP whose mobility is indicated in Figure 2. Isotropic structural factor of aluminum $\eta_s = 10^{-4}$ is also considered.

in resonance frequency is due to the reduction of the Young's modulus and thus of the bending stiffness, whose expression considering this reduction is given in Equation (2). Perforations increase the loss factor

and therefore the added damping compared with the reference by approximately: 1064% for $m, n = 1, 1$; 173% for $m, n = 1, 2$; 126% for $m, n = 2, 1$ and 60% for $m, n = 2, 2$.

The analytical model presented in Section 2 was validated by experimental measurements on MPP in [12].

3. MPP with multi-sized microperforations

3.1. Homogenization model

In this section, an MPP with N group of perforations different perforation diameters denoted d_k with $k = 1, 2, \dots, N$ is considered. Each group of perforations is homogeneously distributed over the MPP which can be considered homogeneous. In order to capture the dynamic response of an MPP with multi-sized perforation diameters, a homogenization approach is proposed. The principle is to model the MPP heterogeneous structure as an equivalent continuous structure. In this context, $2N$ equivalent plates, defined in the same mathematical spacial domain, are considered: N equivalent homogeneous solid plates and N equivalent homogeneous fluid plates as shown in Figure 3 for an MPP with two group of perforation with different perforation diameters. Each homogeneous solid plate is related to its perforations diameter d_k and its corresponding perforation ratio $\phi_k^{(0)}$ ². The fluid flow in each subdomain is independent of the

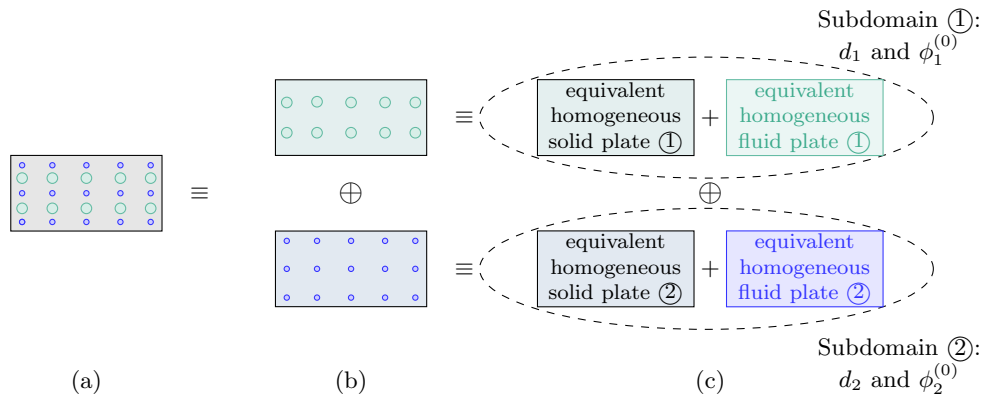


Figure 3: MPP with two groups of perforations with two perforation diameters d_1 and d_2 . The MPP shown in (a) is decomposed into two equivalent MPPs, each associated with a perforation diameter and ratio, as illustrated in (b). The two MPPs in (b) are considered as the sum of two pairs of equivalent homogeneous plates shown in (b) and (c): an equivalent homogeneous fluid plate and an equivalent homogeneous solid plate. Each pair is related to the corresponding d_k and $\phi_k^{(0)}$ with $k = 1$ or 2 .

other subdomains (no direct coupling). The properties of each subdomain (perforation ratio, resistivity) are considered separately. A perforation ratio $\phi_k^{(0)}$ is associated with each perforation diameter d_k and the total perforation ratio is

$$\phi_{\text{tot}}^{(0)} = \sum_{k=1}^N \phi_k^{(0)}. \quad (7)$$

The overall airflow resistivity of the equivalent plate with N perforation diameters takes the form [14, 9, 30]

$$\frac{1}{\sigma} = \sum_{k=1}^N \frac{1}{\sigma_k} \quad (8)$$

where σ_k are given by Equation (4) with $d = d_k$. If $\alpha_\infty \approx 1$, only the resistivity is modified by the addition of perforations of different sizes. For the considered $\phi_{\text{tot}}^{(0)}$, the tortuosity end correction has limited influence on the results. However, in order to account for the size of multiple perforations in the empirical formulation of the length correction tortuosity from [3] given in Equation (5), an average approach is proposed here. The tortuosity is thus rewritten

$$\alpha_\infty = 1 + B_{\text{tot}}(1 - 1.14\sqrt{\phi_{\text{tot}}^{(0)}}) \quad \text{with} \quad B_{\text{tot}} = \frac{1}{\phi_{\text{tot}}^{(0)}} \sum_{k=1}^N \phi_k B_k \quad (9)$$

²Note that the equivalent solid plate of subdomain k is defined by its perforation ratio $\phi_k^{(0)}$. The definition of the global equivalent solid plate is achieved by an electroacoustic analogy [19, 23]. According to this approach, the Young's modulus and density of the overall structure are defined as a function of the overall perforation ratio given in Equation (7).

where B_k defined in Equation (5) are applied to each subdomain k .

The stiffness bending coefficient is also modified in order to capture the effect of the multi-sized microperforation in the dynamic response of the plate. To this end, the stiffness bending correction in Equation (2) becomes a function of $\phi_{\text{tot}}^{(0)}$. Equations (7) to (9) are inserted in Equation (1) to obtain the structural response for an MPP with multi-sized microperforations. Multi-sized microperforations increase the frequency range over which the added damping is effective. As said in Section 2.2, the added damping reaches a maximum at a characteristic frequency that is a function only of the perforation diameter, as defined in Equation (6). Assuming that each added damping phenomenon is independent, the use of N groups of perforations of different diameters induces N characteristic frequencies of maximum damping on the same MPP and thus increases its efficiency. In Figure 4, the thickness of the plate is varied in the range $h \in 0.5 - 3$ mm in order to affect the first and second modes of the plate. Accordingly, the loss factor η_i is obtained as a function of the resonance frequency f_i in Figure 4(a) for $i = 1$ and in Figure 4(b) for $i = 2$. Three configurations are considered in terms of d . In the first one, the perforation diameter d_1 is chosen to induce a maximum added damping on the first natural mode. In the second one, the perforation diameter d_2 is set to maximize the added damping on the second natural mode. In the third configuration, a combination of d_1 and d_2 is considered. The corresponding perforation ratios are $\phi_1^{(0)} = 3\%$ and $\phi_2^{(0)} = 7\%$. For each configuration, the overall perforation ratio defined from Equation (7) is set to 10%. For mode i with $i = 1, 2$, an MPP with a double set of perforations provides similar results

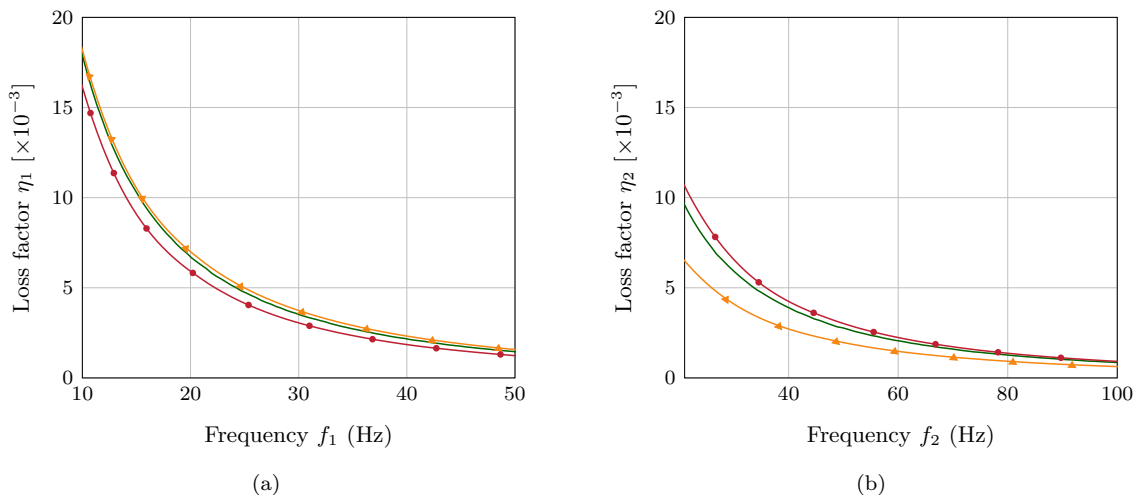


Figure 4: Loss factor for two modes. (a) first mode. (b) second mode. (\blacktriangle) d_1 set to induce a maximal added damping on the first mode with $\phi^{(0)} = 10\%$; (\bullet) d_2 set to maximize the added damping on the second mode with $\phi^{(0)} = 10\%$; (---) combination of d_1 and d_2 with associated perforation ratios $\phi_1^{(0)} = 3\%$ and $\phi_2^{(0)} = 7\%$ where the total perforation ratio defined from Equation (7) is $\phi_{\text{tot}}^{(0)} = \phi_1^{(0)} + \phi_2^{(0)} = 10\%$.

to the case of an MPP with a single set of perforations, where the diameter is chosen to maximize the added damping on the considered mode. The damping induced by the MPP with two group of perforations on mode i is always higher than the one induced on mode k , $i \neq k$, by an MPP with a single set of perforations. As a consequence, a multi-sized perforation MPP does not decrease (or slightly decreases) the added damping efficiency on mode i compared to an MPP where d is chosen to maximize damping on mode i only but allows for efficiency on multiple modes. The perforation ratio of each subdomain also has an influence on the added damping. In fact, mode i is all the more damped as the perforation ratio of the subdomain k is large, with $k \in \mathbb{N}$ is the index of the subdomain. It is therefore possible to adjust $\phi_k^{(0)}$ to maximize the added damping on a mode or to maximize the effect on the N modes.

In order to maximize the added damping in the frequency range between the natural frequencies p and q , the formulation of the perforation diameter of each subdomain, denoted d_p and d_q respectively, is defined as follows

$$d_p = \sqrt{\frac{32\mu_t}{2\pi f_p \rho_t \alpha_\infty}}, \quad (10)$$

where f_p is the natural frequency for the p th mode. A similar expression is given for d_q from f_q . The ω -dependent loss factor $\eta_p(\omega)$ defined by Equation (48) in [12] and the maximum added damping η_p^{max} reached at f_p is calculated. The index p is used for readability reasons, the same is carried out for the index q . The resulting ω function is denoted $\delta_p(\omega)$ for the p index and $\delta_q(\omega)$ for the q th. The absolute difference $\Delta(\omega) = |\delta_p(\omega) - \delta_q(\omega)|$ is plotted in terms of ω . It can be observed that $\Delta(\omega)$ reaches a maximum at a

particular frequency, which is expressed as the geometric mean of f_p and f_q :

$$f_c = \sqrt{f_p f_q}. \quad (11)$$

From the value of f_c given in [Equations \(6\) and \(11\)](#), an estimated σ and thus values for perforation ratio of each subdomain can be estimated numerically.

3.2. Experimental validation

In this section, the experimental validation of the previous approach is performed. The experimental set-up presented is used in [Sections 4 and 5](#). The mechanical parameters of the MPP such as Young's modulus and structural loss factor are determined from the Oberst test bench developed by Mecanum and presented in [Figure 5\(a\)](#). The tested sample is clamped at $x = 0$ and free at $x = L_x$. It is excited by an external force of amplitude F_{ext} at $x = L_x$ and the sample vibratory response is measured by a magnetic sensor located at point R . In order to validate the homogenized model of the multi-sized MPP,

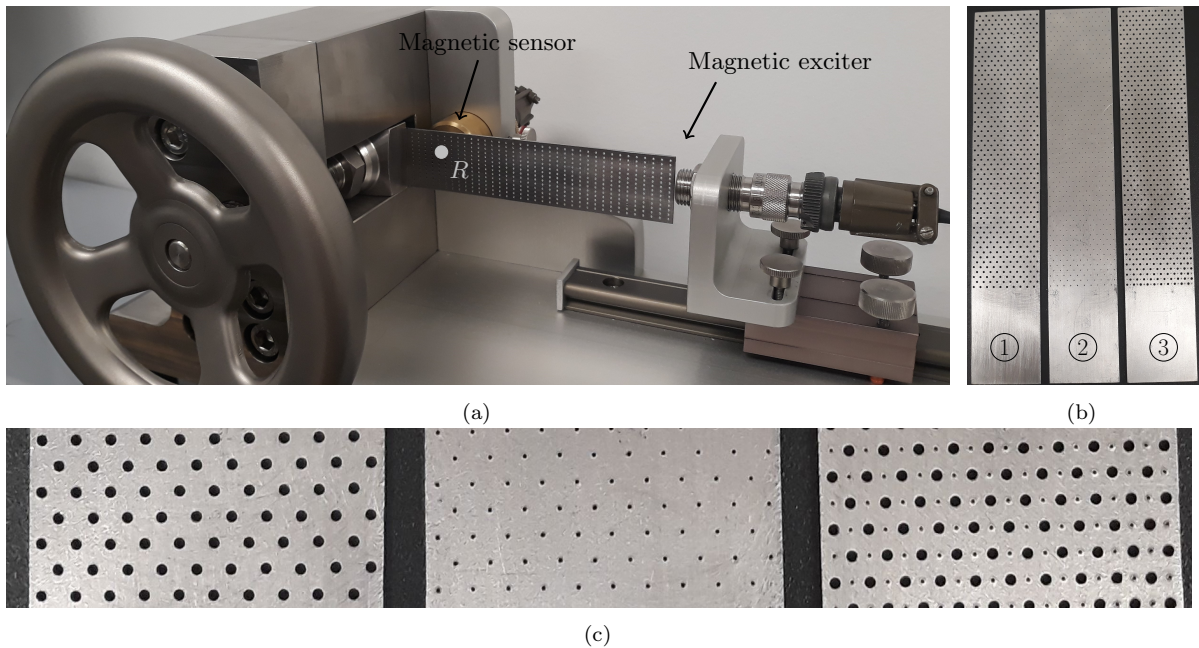


Figure 5: Test bench in [\(a\)](#) and MPP sample in [\(b\)](#) used in the experimental validation of the model presented in [Section 3.1](#). The zoom [\(c\)](#) correspond to a focus on the perforations of [\(b\)](#).

the three samples presented in [Figure 5\(b\)](#) are considered and noted MPP①, MPP② and MPP③. They are made of steel and have a dimension of $130 \text{ mm} \times 30 \text{ mm} \times 0.87 \text{ mm}$. For MPP①, $d \equiv d_1$ is set to induce maximum added damping around the first natural frequency f_1 . For MPP②, $d \equiv d_2$ is chosen to maximize the added damping on the second natural frequency f_2 . The perforation ratios associated with diameters d_1 and d_2 are $\phi_1^{(0)} = 10\%$ and $\phi_2^{(0)} = 2.3\%$ respectively. MPP③ is a combination of MPP① and MPP②. The resulting MPP therefore has two groups of perforation with the two perforation diameters d_1 and d_2 with corresponding perforation ratios $\phi_1^{(0)}$ and $\phi_2^{(0)}$. Moreover, MPP① and MPP② have an equal number of perforations but $d_1 > d_2$ and thus $\phi_1^{(0)} > \phi_2^{(0)}$. MPP③ has therefore the double number of perforations than MPP① and MPP②. The perforation parameters of each MPP are listed in [Table 2](#). The plate mobility, defined as the ratio of the plate velocity at point R to the external

	$\phi_1^{(0)}$ (%)	d_1 (mm)	$\phi_2^{(0)}$ (%)	d_2 (mm)	$\phi_{\text{tot}}^{(0)} = \phi_1^{(0)} + \phi_2^{(0)}$ (%) (7)
MPP①	10	1	.	.	10
MPP②	.	.	2.3	0.4	2.3
MPP③	10	1	2.3	0.4	12.3

Table 2: Measured sample perforation parameters.

force applied to the system F_{ext} , writes $20 \log_{10} |\dot{w}_s / F_{\text{ext}}|$. It is plotted in [Figure 6](#) for the experimental measurements of MPP① and MPP③ and for the analytical results of MPP③. As expected, [Figure 6](#) exhibit a similar amplitude for the first mode between MPP① and MPP③, but it is noted an amplitude reduction of about 3.8 dB on the second resonance frequency between the reference MPP and the MPP

with multiple perforation diameters, i.e., MPP① and MPP③ respectively. It can also be noticed that the model give similar results as the experiments and which validates the model presented in Section 3.1. From the frequency response, which provides the plate mobility as a function of the forced frequency as presented in Figure 6, the loss factor is derived for each considered mode. The loss factor measured

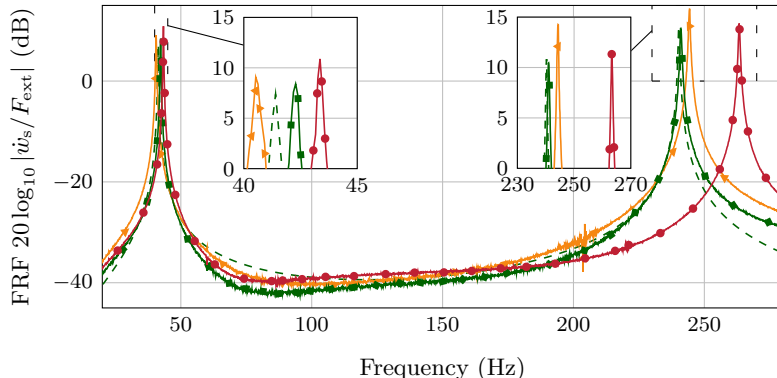


Figure 6: Mobilities for: (—▲) measured MPP① which acts as the reference MPP; (—●) measured MPP②; (—■) measured MPP③; (---) analytical MPP③. Perforation parameters for MPP① and MPP③ are given in Table 2.

for $i = 1, 2$ is depicted in Table 3 for the three MPPs illustrated in Figure 5(b). For MPP③, the loss factor obtained from the theoretical homogenization model presented in Section 3.1 is also provided. Table 3 shows that for MPP③, the damping is maximized for $i = 1$ and $i = 2$ contrary to an MPP with

	Mode 1		Mode 2	
	f_1 (Hz)	$\eta_1 [\times 10^{-3}]$	f_2 (Hz)	$\eta_2 [\times 10^{-3}]$
Measured MPP①	44.2 ± 2.1	0.65 ± 0.002	250.7 ± 3.6	0.14 ± 0.005
Measured MPP②	43.8 ± 0.3	0.34 ± 0.11	260.4 ± 1.9	0.24 ± 0.02
Measured MPP③	43.2 ± 0.5	0.75 ± 0.08	244.2 ± 1.7	0.23 ± 0.002
Analytical MPP③	41.4	0.81	240.3	0.20

Table 3: Values of experimental and theoretical loss factor with standard deviation for the three MPPs presented in Figure 9(a). Each loss factor is determined for the i th mode. Perforation parameters are given in Table 2 for each MPP configurations.

single-sized perforations. The added damping of MPP③ is approximately equal to the sum of the added damping of MPP① and the added damping of MPP②. Using an MPP with a multi-sized perforations increases the frequency band over which the added damping is effective, and can also increase the damping factor of the first modes. Comparison between measured and analytical results obtained for MPP③ in Figure 6 and Table 3 permits to validate the model proposed in Section 3.1.

4. MPP with spacial distribution of perforations

4.1. Perforation ratio gradient

The distribution of the perforations can also have an influence on the added damping. For a given mode, the higher the perforation ratio over the maximum displacement, the higher the added damping. The damping added by the microperforations is due to the viscous friction in the boundary layers of the MPP. This viscous friction is all the more important as the relative velocity of the fluid structure is large. To enhance the added damping effect, it is therefore possible to concentrate the perforations on the antinodes of the modes whose amplitude must be reduced. In this section, only one size of perforation diameter is considered, and the perforation ratio writes as a function of space in order to explore this effect:

$$\phi(x, y) = \phi^{(0)} \mathfrak{h}(x, y) \quad (12)$$

where $\mathfrak{h}(x, y)$ is a normalized inhomogeneity function and $\phi^{(0)}$ the maximum value of the perforation ratio obtained at $\max \mathfrak{h}(x, y) = 1$. The perforation ratio becomes a local variable, however the global perforation ratio ϕ_g is defined by

$$\phi_g = \frac{\phi^{(0)}}{L_x L_y} \int_0^{L_x} \int_0^{L_y} \mathfrak{h}(x, y) dy dx. \quad (13)$$

In Equation (3), D and α_∞ depend on the perforation ratio and become a spacial function by considering the perforation ratio gradient defined in Equation (12). The bending stiffness is given by

$$D(x, y) = \frac{Eh^3}{12(1-\nu^2)} \frac{(1-\phi(x, y))^2}{1+(2-3\nu)\phi(x, y)}, \quad (14)$$

defined from Equation (2) and $\alpha_\infty(x, y) = 1 + B - 1.14B\sqrt{\phi(x, y)}$ where B is defined in Equation (5). Note that the perforation ratio also has an influence on ν [2]. However, for the perforation ratios considered, ν is assumed to be constant [16, 2]. Equations (12) and (14) are inserted into Equation (3) to capture the effect of the perforation ratio gradient in the structural dynamics of MPP. The system of equations describing the autonomous response of a finite MPP saturated by a lightweight fluid in its perforations then becomes

$$D(x, y)\nabla^4 w_s + h(\rho_s(1-\phi(x, y))\ddot{w}_s + \rho_f\phi(x, y)\ddot{w}_f) = 0, \quad (15a)$$

$$\alpha M_f \nabla^2 w_s + \rho_f((1-\alpha_\infty(x, y))\ddot{w}_s + \alpha_\infty(x, y)\ddot{w}_f) + \varsigma(\dot{w}_f - \dot{w}_s) = 0. \quad (15b)$$

In Equation (15), the time and space dependencies of w_s and w_f are dropped for readability purposes. Classical modal analysis is now performed in the same vein as in [?]. The equations must be space semi-discretized and projected onto the non-perforated plate mode. The plate displacement is assumed to be of the form

$$w_s(x, y, t) = \sum_{m=1}^{\infty} \sum_{n=1}^{\infty} w_{mn}^s(t) \Psi_{mn}(x, y), \quad (16)$$

where $w_{mn}^s(t)$ represent the participation of non-perforated plate eigenmode $\Psi_{mn}(x, y)$ determined from boundary conditions. A similar expression holds for the fluid. Equation (16) is rewritten for a finite number of modes and rearranged in lexicographic order according to i . Each pair $(m, n) \in \mathbb{N} \times \mathbb{N}$ corresponds to a single index $i \in \mathbb{N}$. Equation (16) is therefore rewritten in terms of i such that

$$w_s(x, y, t) = \sum_{i=1}^{N_{\text{dof}}} w_i^s(t) \Psi_i(x, y) \quad (17)$$

where N_{dof} is the number of degrees-of-freedom (dof) in plate discretization. The corresponding vector $\Psi(x, y)$ is of size $N_{\text{dof}} \times 1$ and stores the terms $\Psi_i(x, y)$. After this reorganization, Equation (15) are discretized and projected onto the plate and fluid eigenmode basis. To this end, the terms in Equation (15) are multiplied by $\Psi^T(x, y)$ and integrated on the plate surface S . The resulting system is written in the matrix form

$$\dot{\mathbf{z}}(t) = \mathbf{D}\mathbf{z}(t), \quad \text{where } \mathbf{D} = \begin{bmatrix} \mathbf{0} & \mathbf{Id} \\ -\mathbf{M}^{-1}\mathbf{K} & -\mathbf{M}^{-1}\mathbf{C} \end{bmatrix}, \quad \mathbf{z}(t) = \begin{pmatrix} \mathbf{x}(t) \\ \dot{\mathbf{x}}(t) \end{pmatrix} \quad (18)$$

with

$$\mathbf{x}(t) = \begin{pmatrix} \mathbf{w}_s(t) \\ \mathbf{w}_f(t) \end{pmatrix}; \quad \mathbf{M} = \begin{bmatrix} \mathbf{M}_{s_1} & \mathbf{M}_{f_1} \\ \mathbf{M}_{s_2} & \mathbf{M}_{f_2} \end{bmatrix}; \quad \mathbf{C} = \begin{bmatrix} \mathbf{0} & \mathbf{0} \\ \mathbf{C}_{s_2} & \mathbf{C}_{f_2} \end{bmatrix}; \quad \mathbf{K} = \begin{bmatrix} \mathbf{K}_{s_1} & \mathbf{0} \\ \mathbf{K}_{s_2} & \mathbf{0} \end{bmatrix}. \quad (19)$$

The displacement contributions of the solid are stored in \mathbf{w}_s and those of the fluid, in \mathbf{w}_f . Each matrix of Equation (19) is written as follows :

$$\begin{aligned} \mathbf{M}_{s_1} &= h\rho_s \iint_S (1-\phi(x, y)) \Psi \Psi^T dx dy, & \mathbf{M}_{s_2} &= \rho_f \iint_S (1-\alpha_\infty(x, y)) \Psi \Psi^T dx dy, \\ \mathbf{M}_{f_1} &= h\rho_f \iint_S \phi(x, y) \Psi \Psi^T dx dy, & \mathbf{M}_{f_2} &= \rho_f \iint_S \alpha_\infty(x, y) \Psi \Psi^T dx dy, \\ \mathbf{C}_{s_2} &= -\varsigma \iint_S \Psi \Psi^T dx dy, & \mathbf{C}_{f_2} &= \varsigma \iint_S \Psi \Psi^T dx dy, \\ \mathbf{K}_{s_1} &= \iint_S D(x, y) \nabla^4 \Psi \Psi^T dx dy & \mathbf{K}_{s_2} &= \alpha M_f \iint_S \nabla^2 \Psi \Psi^T dx dy. \end{aligned} \quad (20)$$

An analytical solution of the equation of motion is possible in the state space. Solutions for the i th mode take the form of eigenvalues $\lambda_i = \beta_i \pm j\gamma_i$ where $\beta_i = -\zeta_i/\omega_i$ is the damping term involved into the exponential decrease of the mode due to viscous friction with ζ_i is the modal damping factor. The imaginary part $\gamma_i = \omega_i\sqrt{1-\zeta_i^2}$ corresponds to the natural frequency, where ω_i is the undamped frequency. The loss factor is related to ζ_i by the following expression: $\eta_i = 2\zeta_i$.

In order to explore the influence of the spacial distribution of the perforation on the added damping, the loss factor of the first mode η_1 is plotted as a function of the global perforation ratio in Figure 7.

Three spacial distributions are considered:

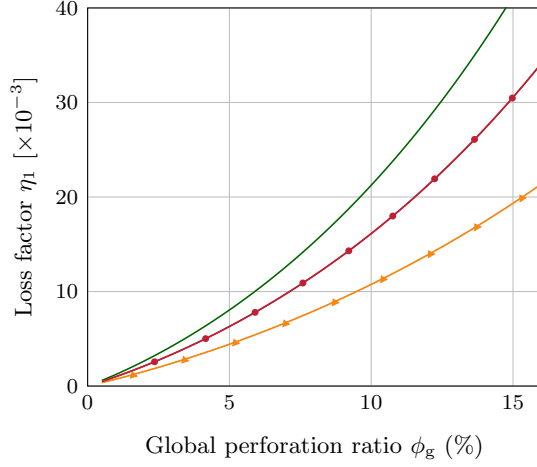


Figure 7: Loss factor for the first mode of a 570 mm \times 490 mm \times 1 mm simply-supported aluminum MPP with $d = 1.4$ mm: (\blacktriangle) uniform distribution with $\text{lh}(x, y) = 1$; (\bullet) distribution along plate mode shape according x with $\text{lh}(x, y) = \sin(\pi x/L_x)$; (—) distribution according to the rectangular function $\text{lh}(x, y) = \Pi(x)$ defined in Equation (21).

Configuration 4 The perforations are homogeneously distributed on the MPP and correspond to the reference MPP, i.e. $\text{lh}(x, y) = 1$.

Configuration 5 The perforations are distributed according to the shape of the first plate mode without perforation thus $\text{lh}(x, y) = \sin(\pi x/L_x)$. The normalized inhomogeneity function is equal to 1 at the maximum plate deflection. The spacial perforation ratio is defined via Equation (12).

Configuration 6 The perforations are distributed according to the step function

$$\text{lh}(x, y) = \Pi(x) = \begin{cases} 1 & \text{if } \frac{1}{4} \leq \frac{x}{L_x} \leq \frac{3}{4}, \\ 0 & \text{else.} \end{cases} \quad (21)$$

As previously mentioned, the added damping exhibited by MPPs is closely related to the viscous friction in the boundary layers of the MPPs, which is more important the higher the relative velocity of the fluid structure. Adapted from [5] for an MPP with inhomogeneous spacial distribution of perforation under low frequency assumptions, the viscous friction force can be recast as

$$f_v(x, y, t) = \frac{32\mu_f\phi(x, y)}{d^2}(\dot{w}_f(x, y, t) - \dot{w}_s(x, y, t)). \quad (22)$$

The larger the velocity difference, the greater the friction force. From the discretization in Equation (17), Equation (22) reads

$$f_v(x, y, t) = \frac{32\mu_f\phi(x, y)}{d^2} \sum_i^{N_{\text{dof}}} \Psi_i(x, y)(\dot{w}_i^f(t) - \dot{w}_i^s(t)). \quad (23)$$

For a given mode, maximizing $\Psi_i(x, y)$ leads to maximizing the friction force and thus the additional damping of the MPP. Values of x and y for which $\Psi_i(x, y)$ reaches a maximum can be obtained depend on the size of the plate and on the boundary conditions involved in defining the eigenfunction. For a given d , the viscous force and, thus, the additional damping induced by the microperforations, is maximal for the i th mode when $x = x_{\text{max}}$ is the solution of $\partial_x \Psi_i(x, y) = 0$ and when $y = y_{\text{max}}$ is the solution of $\partial_y \Psi_i(x, y) = 0$. The added damping increases with the perforation ratio. It is therefore possible to increase the added damping by increasing the perforation ratio around the point $(x_{\text{max}}, y_{\text{max}})$. However, the concentration of perforations on the zones of interest, i.e. presenting maximum deflection amplitudes, will have a lower mechanical resistance, due to the modification of the Young's modulus. In addition, the more abrupt the change, the greater the stress concentrations at the point of failure, which reduces the mechanical strength of the structure.

Moreover, the spacial distribution of the perforation has an influence on the Young modulus of the structural part and thus on the MPP stiffness. For the first MPP mode of the three MPP represented in Figure 7, the space-dependent Young modulus $E(x, y)$ given in Equation (14) is plotted versus ϕ_g in Figure 8. For the same ϕ_g , $E(x, y)$ decreases significantly when the concentration of perforations is shifted to the maximum deflection area of the plate.

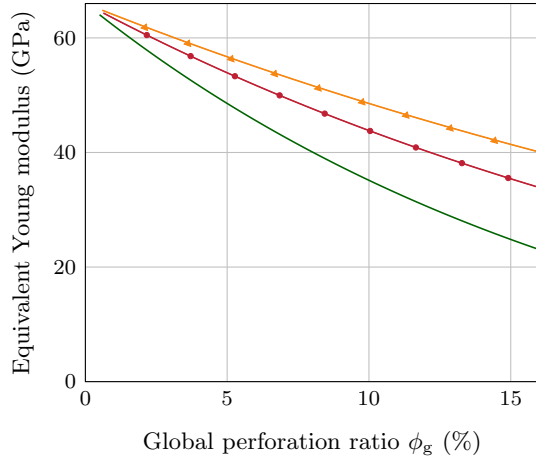


Figure 8: Space-dependent Young’s modulus $E(x, y)$ given in Equation (14) for the first mode of a $570 \text{ mm} \times 490 \text{ mm} \times 1 \text{ mm}$ simply-supported aluminum MPP with $d = 1.4 \text{ mm}$ as a function of the global perforation ratio ϕ_g for three different spacial perforation distributions: (—▲) uniform distribution with $\text{Ih}(x, y) = 1$; (—●) distribution along plate mode shape according x with $\text{Ih}(x, y) = \sin(\pi x/L_x)$; (—) distribution according to the rectangular function $\text{Ih}(x, y) = \Pi(x)$ defined in Equation (21).

4.2. Experimental validation

In this section, the experimental validation is performed on the Oberst test bench detailed in Section 3.2. The tested MPP samples are presented in Figure 9(a) and measure $131 \text{ mm} \times 30.7 \text{ mm} \times 1.08 \text{ mm}$. The overall perforation ratio and the diameter of the perforations are constant for the three plates and fixed at $\phi_g = 10\%$ and $d = 1 \text{ mm}$, respectively. For MPP④ the perforations are homogeneously distributed over the structure. In this validation section, MPP④ acts as the MPP reference. For MPP⑤, the perforation ratio is chosen as a linear function of x with a maximum $x = L_x$ (maximum plate deflection for the first mode) such that $\phi(x) = \phi^{(0)}x/L_x$ with $\phi^{(0)} = 20\%$. For MPP⑥, the perforation ratio is defined by

$$\phi(x) = \phi^{(0)}\Pi(x) \quad \text{with} \quad \Pi(x) \begin{cases} 1 & \text{if } \frac{x}{L_x} \geq \frac{1}{2}, \\ 0 & \text{else.} \end{cases} \quad (24)$$

where $\phi^{(0)} = 20\%$. All perforation parameters and $\text{Ih}(x)$ homogeneity functions for the three MPPs of Figure 9(a) previously presented are reported in Figure 9(b). Experimental results are presented in Figure 10 and Table 4. In Figure 10, the plate mobility for the first mode of MPP⑤ and MPP⑥ are compared to that obtained for the MPP reference (MPP④) and the non-perforated plate reference ①. An amplitude reduction of about 10 dB is observed between the two MPPs with spatial distribution of perforations (i.e., MPP⑤ and MPP⑥) and the non-perforated plate. The amplitude reduction between MPPs with spacial distribution and the reference MPP is about 3 dB. The resonance frequency is shifted due to the reduction in stiffness, which is greater for MPP⑥ than MPP⑤ and than the reference MPP④.

Comparisons between measurements and theories for MPP⑤ and MPP⑥ are given in Figure 10 and validate the analytical model presented in Section 4.1. From the plate mobility in Figure 10, the loss factor for each mode i , with $i \leq 5$, is calculated. The results are given in Table 4 for the tested samples and the reference non-perforated plate ①. In addition, the Section 4.1 model was also considered for calculating the loss factor of the first mode (i.e., $i = 1$) for the three MPPs. Experimental and theoretical loss factor for the first mode and their corresponding resonance frequency are indicated in Table 4. For

	Measured		Analytical	
	f_1 (Hz)	$\eta_1 [\times 10^{-3}]$	f_1 (Hz)	$\eta_1 [\times 10^{-3}]$
Reference non-perforated plate ①	47.9 ± 0.36	0.9 ± 0.073	.	.
MPP④	48.1 ± 0.12	1.3 ± 0.075	47.2	1.2
MPP⑤	48.4 ± 0.50	1.7 ± 0.190	46.5	1.6
MPP⑥	48.0 ± 1.97	2.1 ± 0.079	45.8	2.0

Table 4: Measured with standard deviation and analytical frequencies of the first mode plate and corresponding loss factors for the reference non-perforated plate ① and the three MPPs presented in Figure 9(a) and perforation parameters are given in Table 2. Theoretical results obtained though the model proposed in Section 4.1 provided for $i = 1$.

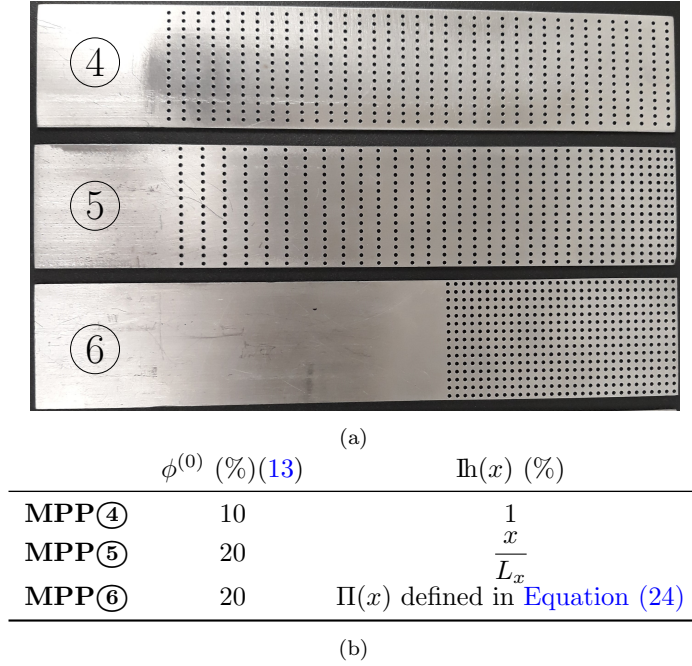


Figure 9: Tested MPP samples with various space-dependent distributions of the perforation ratio. (a) — MPP ④ homogeneous distribution: reference MPP, MPP ⑤ linear distribution, MPP ⑥ concentrated distribution located at the maximum of the deflection amplitude. (b) — Perforation parameters and homogeneity function $\text{Ih}(x)$ for the three MPPs presented in Figure 9(a). Perforation diameter is set to $d = 1$ mm in order to induce maximum damping around the first mode (i.e. $i = 1$) and global perforation ratio $\phi_g = 10\%$ identical for all three MPP.

the same overall perforation ratio, distributing the perforations over the maximum deflection areas of the MPP can increase the added damping by 62% over the reference MPP and 133% over the non-perforated plate. However, a large concentration of perforations in a small area generates a stress concentration that reduces the mechanical strength of the structure. This aspect must be carefully considered when designing the MPP. In this regard, it is possible in practice to patch the perforations on the vibration bellies of the modes that one wishes to attenuate.

5. MPP with multi-sized perforations and spacial distribution of perforations

In this section, it is proposed to explore the damping capabilities of the MPP with a spatial distribution of multi-size perforations; both presented in Sections 3 and 4. The idea is to design an MPP that improves the frequency range of the effective damping while maximizing the added damping on the frequencies of interest, i.e. the resonance frequencies of the structure. Both analytical models exposed in Sections 3 and 4 are combined to obtain the dynamic response of an MPP involving space-dependent distributions of multi-sized perforations. The MPP is assumed to be equivalent to N independent MPPs, each with its own perforation diameter d_k , perforation ratio $\phi_k^{(0)}$, and inhomogeneity function Π_k , $k = 1, 2, \dots, N$. Based on a homogenization model similar to the one presented in Section 3, the equations of motion generalize to (time and space dependencies are dropped out for the purpose of readability)

$$D(x, y) \nabla^4 w_s + h(\rho_s(1 - \phi(x, y)) \ddot{w}_s + \rho_f \phi(x, y) \ddot{w}_f) = 0 \quad (25a)$$

$$\alpha M_f \nabla^2 w_s + \rho_f((1 - \alpha_\infty(x, y)) \ddot{w}_s + \alpha_\infty(x, y) \ddot{w}_f) + \sigma(x, y) \phi(x, y) (\dot{w}_f - \dot{w}_s) = 0 \quad (25b)$$

with

$$\frac{1}{\sigma(x, y)} = \sum_{k=1}^N \frac{1}{\sigma_k(x, y)}. \quad (26)$$

The spacial bending coefficient $D(x, y)$ is expressed in terms of the overall perforation ratio $\phi(x, y)$ defined through Equation (7) applied to $\phi_k(x, y)$. The global spacial resistivity $\sigma(x, y)$ is defined from the resistivity of each equivalent plate derived from d_k and $\phi_k(x, y)$. The overall spacial tortuosity is also expressed using Equation (9) applied to the spacial perforation ratio $\phi_k(x, k)$ and the perforation diameter of the subdomain k . The validation of the generalized model in Equation (25) is now exposed. To this aim, two plates of dimension $195 \text{ mm} \times 30.7 \text{ mm} \times 1.17 \text{ mm}$ are considered: a non-perforated reference plate ②

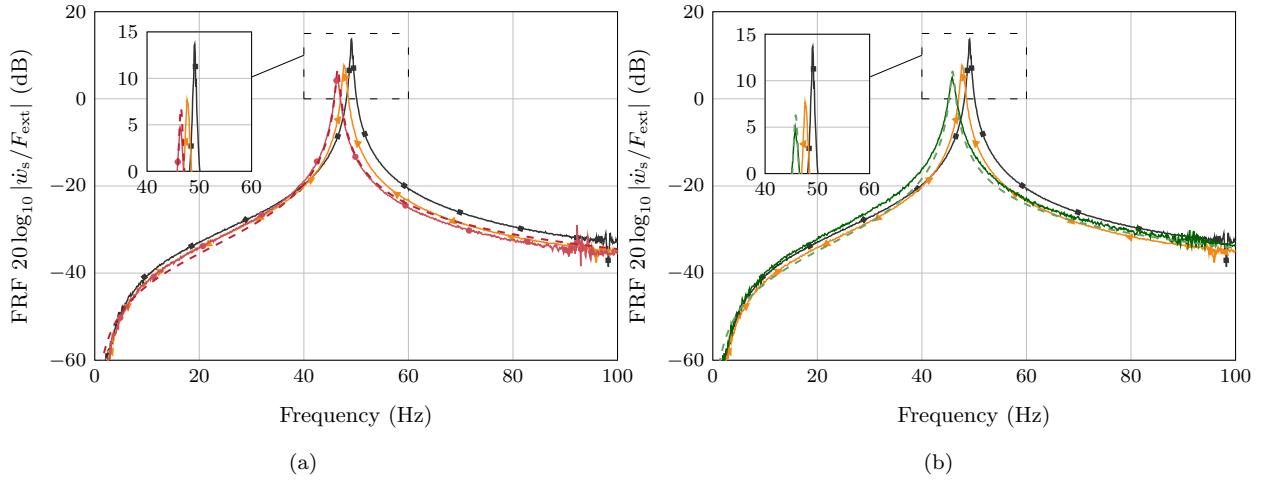


Figure 10: Theoretical and experimental mobilities: MPP⑤ in (a) with: (—●—) measured; (---) theoretical, and for MPP⑥ in (b) with: (---) measured; (—) theoretical. In (a) and (b) the reference MPP (—▲—) and the reference non-perforated plate (—■—) are provided. Mobilities of MPP with spatial distribution are compared to the reference non-perforated plate ① and the reference MPP; i.e., MPP④ in Figure 9(a). MPP perforation parameters are given in Figure 9(b).

and MPP⑦ with multiple perforation diameters spatially distributed along a non-homogeneous pattern. In order to maximize the damping added by the microperforations on modes 1 and 2, two diameters of perforations are chosen: $d_1 = 1.3$ mm which corresponds to $f_{c_1} \approx 27$ Hz and $d_2 = 0.7$ mm which refers to $f_{c_2} \approx 114$ Hz. MPP⑦ which is presented in Figure 11 is decomposed into three equivalent plates with respective perforation ratios and inhomogeneity functions defined below:

$$\phi_1(x) = \phi_1^{(0)} \Pi_1(x) \quad \text{with} \quad \Pi_1(x) = \begin{cases} 1 & \text{if } \frac{x}{L_x} \geq 0.695, \\ 0 & \text{otherwise} \end{cases} \quad \text{and} \quad \phi_1^{(0)} = 33\%, \quad (27a)$$

$$\phi_2(x) = \phi_2^{(0)} \Pi_2(x) \quad \text{with} \quad \Pi_2(x) = \begin{cases} 1 & \text{if } \frac{x}{L_x} \geq 0.8, \\ 0 & \text{otherwise} \end{cases} \quad \text{and} \quad \phi_2^{(0)} = 11\%, \quad (27b)$$

$$\phi_3(x) = \phi_3^{(0)} \Pi_3(x) \quad \text{with} \quad \Pi_3(x) = \begin{cases} 1 & \text{if } 0.165 \leq \frac{x}{L_x} \leq 0.695, \\ 0 & \text{otherwise} \end{cases} \quad \text{and} \quad \phi_3^{(0)} = 16\%. \quad (27c)$$

The ratio $\phi_1(x)$ is associated with perforations of diameter, d_1 while $\phi_2(x)$ and $\phi_3(x)$ are related to

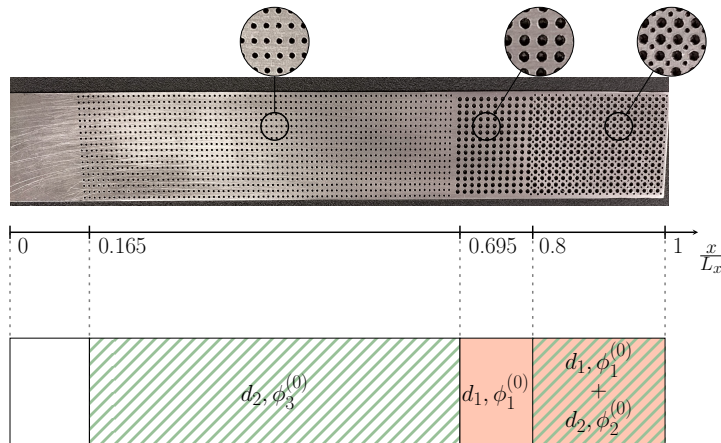


Figure 11: MPP⑦: spacial perforation distribution described in Equation (27).

perforations of diameter d_2 . The test bench described in Section 3.2 is used to obtain the MPP mobility, as shown in Figure 12. The mobility measured for the MPP is compared to that of the reference non-perforated plate ② and the analytical mobility calculated for the MPP. Figure 12 exhibits a magnitude reduction of about 12 dB on the first resonance frequency, while the magnitude reduction is about 10 dB for the second resonance frequency. The loss factor increases by 98% on the first resonance frequency and by 93% on the second one in the case of MPP⑦ compared to the non-perforated plate case. Altogether,

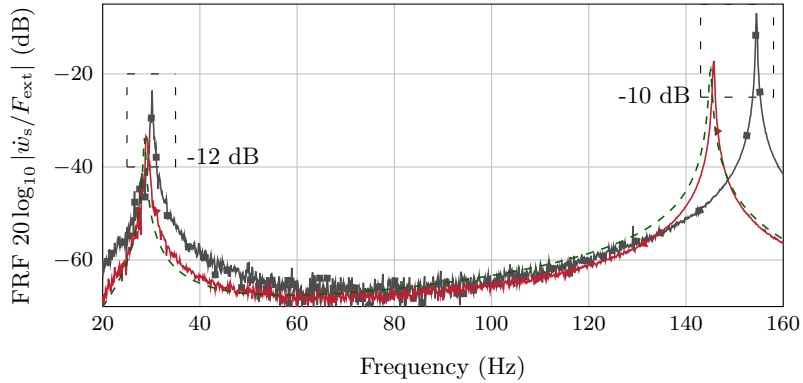


Figure 12: Plate mobility in dB with: (\blacktriangle) measured MPP⑦ shown in Figure 11, (\blacksquare) measured reference non-perforated plate ② and ($---$) theoretical MPP⑦. MPP⑦ is considered as three equivalent MPP inhomogeneous spacial distribution of perforations defined in Equation (27). Spacial distribution (27a) associated with $d_1 = 1.3$ mm while spacial distributions (27b) and (27c) are related to $d_2 = 0.7$ mm. Loss factor and Young’s modulus used in the theoretical model are obtained experimentally from measurements on the non-perforated plate.

	Mode 1		Mode 2	
	f_1 (Hz)	$\eta_1 [\times 10^{-3}]$	f_2 (Hz)	$\eta_2 [\times 10^{-3}]$
Measured reference non-perforated plate ②	33.41	0.63	147.7	0.15
Measured MPP⑦	31.41	1.26	142.4	0.29
Analytical MPP⑦	28.6	1.25	145.1	0.25

Table 5: Values of experimental and theoretical loss factor for the MPP⑦ presented in Figure 11. Each loss factor is determined for the i th mode. Perforation are described in Equation (27).

we can state that the implementation of multi-sized microperforations combined with inhomogeneous spacial distributions of perforations has two advantages: (1) depending on the diameters chosen, the added damping is effective over a wider frequency band compared to a plate with a single set of perforations; (2) the well-chosen distribution of the perforations over certain areas of interest also maximizes the added damping.

6. Conclusion

This paper proposed as an extension of [12] to study the added damping effect exhibited by microperforated plates (MPPs) embedding: (i) multi-sized perforations diameters; (ii) spacial distributions of perforation; (iii) a combination of (i) and (ii) that corresponds to spacial distributions of multi-sized perforation diameters. For this purpose, it was proposed a homogenization approach in the context of MPPs with multi-sized perforations. Then, in order to consider an MPP with a spacial distribution of microperforations, the perforation ratio was introduced as a space-dependent function. Finally, these two models were combined. Experimental measurements validate the analytical models. Results provide evidence that:

(i) MPPs with multiple perforations can broaden the frequency band of the effective added damping. When the perforation diameters are chosen so that each characteristic frequency coincides with a resonance frequency of the MPP, the frequency band of the effective damping is extended.

(ii) MPPs with spatial distribution of perforations can maximize the added damping on one mode. Indeed, the distribution of perforations around the antinodes of the considered mode maximizes the added damping compared to a homogeneous MPP.

(iii) the two effects can be cumulated for MPP with multi-sized perforation diameters and spatial distribution of perforations. The combination of multiple perforation sizes with inhomogeneous spacial distribution of perforations had the two main advantages of increasing the frequency band over which added damping was actually effective and maximizing the added damping over several properly selected frequencies.

Practically, the perforations could be distributed through patches located on the vibration antinodes of the plate modeshape to be damped.

CRediT authorship contribution statement

Lucie Gallerand: Conceptualization, Methodology, Software, Validation, Writing - original draft, Writing - review & editing. **Mathias Legrand:** Conceptualization, Methodology, Supervision, Writing - original draft, review & editing. **Thomas Dupont:** Conceptualization, Methodology, Supervision, Resources, Funding acquisition, Writing - original draft, review & editing. **Philippe Leclaire:** Conceptualization, Methodology, Supervision, Writing - original draft, review & editing.

Supplementary material

Python scripts used to perform the modal analysis presented in this article are available in commit 292f7864 of the [\[Git repository\] Inhomogeneous Perforated Plate](#)

Acknowledgment

This work was supported by the Natural Sciences and Engineering Research Council of Canada (NSERC) and by Fonds de recherche du Québec - Nature et technologies (FRQNT) program financing through the project of the reference number RGPIN-2019-06573.

References

- [1] T. Adams. *Sound materials: A compendium of sound absorbing materials for architecture and design*. Frame Publishers, 2017. ISBN: 978-94-923-1153-5.
- [2] M. Arnold, A. R. Boccaccini, and G. Ondracek. Prediction of the poisson's ratio of porous materials. *Journal of Materials Science*, 31(6):1643–1646, 1996. [\[DOI\]](#).
- [3] N. Atalla and F. Sgard. Modeling of perforated plates and screens using rigid frame porous models. *Journal of Sound and Vibration*, 303:195–208, 2007. [\[DOI\]](#), [\[OA\]](#).
- [4] M.A. Biot. Theory of propagation of elastic waves in a fluid-saturated porous solid. I. Low-frequency range. *Journal of the Acoustical Society of America*, 28(2):168–178, 1956. [\[DOI\]](#), [\[OA\]](#).
- [5] M.A. Biot. Theory of propagation of elastic waves in a fluid-saturated porous solid. II. Higher frequency range. *Journal of the Acoustical Society of America*, 28(2):179–191, 1956. [\[DOI\]](#), [\[OA\]](#).
- [6] A.R. Boccaccini and Z. Fan. A new approach for the Young's modulus-porosity correlation of ceramic materials. *Ceramics International*, 23(3):239–245, 1997. [\[DOI\]](#).
- [7] T. Bravo, C. Maury, and C. Pinhède. Vibroacoustic properties of thin micro-perforated panel absorbers. *Journal of the Acoustical Society of America*, 132:789–798, 2012. [\[DOI\]](#).
- [8] J. Carbajo, J. Ramis, L. Godinho, and P. Amado-Mendes. Assessment of methods to study the acoustic properties of heterogeneous perforated panel absorbers. *Applied Acoustics*, 133:1–7, 2018. [\[DOI\]](#).
- [9] J. Carbajo, J. Ramis, L. Godinho, and P. Amado-Mendes. Perforated panel absorbers with micro-perforated partitions. *Applied Acoustics*, 149:108–113, 2019. [\[DOI\]](#).
- [10] Y. Champoux and M.R. Stinson. On acoustical models for sound propagation in rigid frame porous materials and the influence of shape factors. *Journal of the Acoustical Society of America*, 92:1120–1131, 1992. [\[DOI\]](#).
- [11] T. Dupont, G. Pavic, and B. Laulagnet. Acoustic properties of lightweight micro-perforated plate systems. *Acta Acustica united with Acustica*, 89(2):201–212, 2003. [\[OA\]](#).
- [12] L. Gallerand, M. Legrand, T. Dupont, and P. Leclaire. Vibration and damping analysis of a thin finite-size microperforated plate. *Journal of Sound and Vibration*, 541:117295, 2022. [\[DOI\]](#), [\[OA\]](#).
- [13] K. Hoshi, T. Hanyu, T. Okuzono, K. Sakagami, M. Yairi, S. Harada, S. Takahashi, and Y. Ueda. Implementation experiment of a honeycomb-backed MPP sound absorber in a meeting room. *Applied Acoustics*, 157:107000, 2020. [\[DOI\]](#).
- [14] K. H. Kim and G. H. Yoon. Absorption performance optimization of perforated plate using multiple-sized holes and a porous separating partition. *Applied Acoustics*, 120:21–33, 2017. [\[DOI\]](#).
- [15] P. Leclaire, K.V. Horoshenkov, and A. Cummings. Transverse vibration of a thin rectangular porous plate saturated by a fluid. *Journal of Sound and Vibration*, 247(1):1–18, 2001. [\[DOI\]](#), [\[OA\]](#).
- [16] M. P. Lutz and R. W. Zimmerman. The effect of pore shape on the poisson ratio of porous materials. *Mathematics and Mechanics of Solids*, 26(8):1191–1203, 2021. [\[DOI\]](#).
- [17] D.-Y. Maa. Microperforated-panel wideband absorbers. *Noise Control Engineering Journal*, 29(3):77, 1987. [\[DOI\]](#).
- [18] L. Maxit, C. Yang, L. Cheng, and J.-L. Guyader. Modeling of micro-perforated panels in a complex vibro-acoustic environment using patch transfer function approach. *Journal of the Acoustical Society of America*, 131(3):2118–2130, 2012. [\[DOI\]](#).
- [19] I.M. Miasa, M. Okuma, G. Kishimoto, and T. Nakahara. An Experimental Study of a Multi-Size Microperforated Panel Absorber. *Journal of System Design and Dynamics*, 1(2):331–339, 2007. [\[DOI\]](#).
- [20] A.I. Mosa, A. Putra, R. Ramlan, I. Prasetyo, and A. Esraa. Theoretical model of absorption coefficient of an inhomogeneous MPP absorber with multi-cavity depths. *Applied Acoustics*, 146:409–419, 2019. [\[DOI\]](#).
- [21] M. Ouisse, L. Maxit, C. Cacciolati, and J.-L. Guyader. Patch transfer functions as a tool to couple linear acoustic problems. *Journal of Vibration and Acoustics*, 127(5):458–466, 2004. [\[DOI\]](#).

- [22] A. Putra, Y. M. Cheah, N. Muhammad, A. Rivai, and C. M. Wai. The effect of perforation on the dynamics of a flexible panel. *Advances in Acoustics and Vibration*, 2014:1–17, 2014. [\[DOI\]](#).
- [23] Y. Qian and K. Zhang. Influence of arranged patterns on the absorption performance of parallel MPP absorbers. *Applied Acoustics*, 192:108701, 2022. [\[DOI\]](#).
- [24] Y.J. Qian, K. Cui, S.M. Liu, Z.B. Li, D.S. Shao, D.Y. Kong, and S.M. Sun. Optimization of multi-size micro-perforated panel absorbers using multi-population genetic algorithm. *Noise Control Engineering Journal*, 62(1):37–46, 2014. [\[DOI\]](#).
- [25] H. Ruiz, P. Cobo, and F. Jacobsen. Optimization of multiple-layer microperforated panels by simulated annealing. *Applied Acoustics*, 72(10):772–776, 2011. [\[DOI\]](#).
- [26] D. Takahashi and M. Tanaka. Flexural vibration of perforated plates and porous elastic materials under acoustic loading. *Journal of the Acoustical Society of America*, 112(4):1456–1464, 2002. [\[DOI\]](#).
- [27] M.A. Temiz, J. Tournadre, I.L. Arteaga, P. Martínez-Lera, and A. Hirschberg. Modelling vibro-acoustic coupling in flexible micro-perforated plates by a patch-impedance approach. *Applied Acoustics*, 125:80–90, 2017. [\[DOI\]](#).
- [28] L. Wang and T. Wang. Investigation of the effect of perforated sheath on thermal-flow characteristics over a gas turbine reverse-flow combustor—Part 2: Computational analysis. *Journal of Thermal Science and Engineering Applications*, 12(4), 2019. [\[DOI\]](#), [\[OA\]](#).
- [29] M.Q. Wu. Micro-perforated panels for duct silencing. *Noise Control Engineering Journal*, 45(2):69–77, 1997. [\[DOI\]](#), [\[OA\]](#).
- [30] B. Zhang, S. Lang, P. Ge, and W. Zhuang. The study of sound absorption characteristic of micro-perforated panel with different diameter holes. In *29th International Congress and Exhibition on Noise Control Engineering (internoise 2000)*, 2000. [\[OA\]](#).